

Conversion Reaction Mechanisms in Lithium Ion Batteries: Study of the Binary Metal Fluoride Electrodes

Feng Wang,[†] Rosa Robert,[‡] Natasha A. Chernova,[§] Nathalie Pereira,^{||} Fredrick Omenya,[§] Fadwa Badway,^{||} Xiao Hua,[†] Michael Ruotolo,^{||} Ruigang Zhang,[§] Lijun Wu,[†] Vyacheslav Volkov,[†] Dong Su,[†] Baris Key,[†] M. Stanley Whittingham,[§] Clare P. Grey,^{‡,†} Glenn G. Amatucci,^{||} Yimei Zhu,[†] and Jason Graetz^{*†}

[†]Brookhaven National Laboratory, Upton, New York 11973, United States

[‡]Chemistry Department, University of Cambridge, Lensfield Road, Cambridge, CB2 1EW, United Kingdom

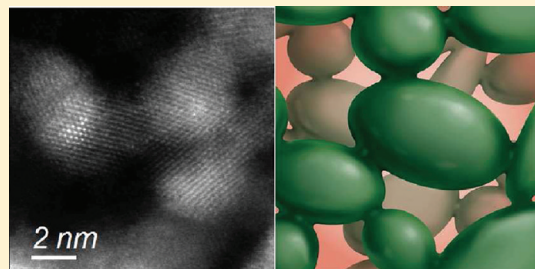
[§]Materials Science and Engineering, State University of New York at Binghamton, Binghamton, New York 13902-6000, United States

^{||}Department of Materials Science and Engineering, Energy Storage Research Group, Rutgers University, North Brunswick, New Jersey 08902, United States

[†]Chemistry Department, Stony Brook University, Stony Brook, New York 11794-3400, United States

 Supporting Information

ABSTRACT: Materials that undergo a conversion reaction with lithium (e.g., metal fluorides MF_2 : $M = Fe, Cu, \dots$) often accommodate more than one Li atom per transition-metal cation, and are promising candidates for high-capacity cathodes for lithium ion batteries. However, little is known about the mechanisms involved in the conversion process, the origins of the large polarization during electrochemical cycling, and why some materials are reversible (e.g., FeF_2) while others are not (e.g., CuF_2). In this study, we investigated the conversion reaction of binary metal fluorides, FeF_2 and CuF_2 , using a series of local and bulk probes to better understand the mechanisms underlying their contrasting electrochemical behavior. X-ray pair-distribution-function and magnetization measurements were used to determine changes in short-range ordering, particle size and microstructure, while high-resolution transmission electron microscopy (TEM) and electron energy-loss spectroscopy (EELS) were used to measure the atomic-level structure of individual particles and map the phase distribution in the initial and fully lithiated electrodes. Both FeF_2 and CuF_2 react with lithium via a direct conversion process with no intercalation step, but there are differences in the conversion process and final phase distribution. During the reaction of Li^+ with FeF_2 , small metallic iron nanoparticles (<5 nm in diameter) nucleate in close proximity to the converted LiF phase, as a result of the low diffusivity of iron. The iron nanoparticles are interconnected and form a bicontinuous network, which provides a pathway for local electron transport through the insulating LiF phase. In addition, the massive interface formed between nanoscale solid phases provides a pathway for ionic transport during the conversion process. These results offer the first experimental evidence explaining the origins of the high lithium reversibility in FeF_2 . In contrast to FeF_2 , no continuous Cu network was observed in the lithiated CuF_2 ; rather, the converted Cu segregates to large particles (5–12 nm in diameter) during the first discharge, which may be partially responsible for the lack of reversibility in the CuF_2 electrode.



INTRODUCTION

The cathodes used in commercial lithium batteries are typically intercalation compounds (e.g., $LiCoO_2$, $LiFePO_4$), wherein lithium is inserted and removed from planes or tunnels in the host structure. While these topotactic reactions ensure good reversibility, they have a limited capacity, which is set by the number of available lithium sites. Because of their moderate energy density, these materials are not likely to meet the growing demand for rapidly miniaturizing electronics and large-scale mobile devices (e.g., electric vehicles). One route to achieving a larger specific capacity is to utilize all possible oxidation states of a compound through a conversion reaction in which more than one electron transfer occurs per transition metal (TM) ion, as opposed to

0.5–1.0 electrons, which is typical for intercalation compounds. The demonstration of a reversible lithium conversion reaction in TM oxides renewed interest in conversion compounds as high-capacity electrodes.^{1,2} In addition to the oxides, other conversion compounds of interest include hydrides, sulfides, nitrides, and fluorides.^{3–6} The reaction potentials of these systems scale with the electronegativity of the anion and span a wide range. However, only fluorides have sufficiently high reaction potentials to be suitable as cathodes. Nevertheless, problems with poor kinetics, cycle life, and reversibility are only some of the

Received: July 6, 2011

challenges that hinder the potential commercialization of these electrodes.^{2,7}

Despite decades of effort and intense recent interest, the mechanisms underpinning the conversion reactions are not well understood.^{8,9} In the few systems exhibiting reversibility, such as metal oxides and fluorides, their good cycling characteristics are attributed to the *in situ* formation of fine metallic nanoparticles embedded in an insulating matrix (e.g., Li₂O or LiF). Purportedly, this configuration allows for rapid mass transport since the diffusion distances remain short during the redox process.¹ However, it is interesting to note that conversion electrodes prepared in the lithiated state (e.g., LiF + M), by mechanically mixing metallic nanoparticles with the lithium compound, are electrochemically inactive (aside from a small amount of capacity in grain boundaries at low voltages).¹⁰ It remains unclear exactly what happens during the first lithiation that facilitates subsequent cycling. Similarly, little is known about origins of the asymmetric lithiation/delithiation reaction paths, the large polarization and hysteresis, and why some materials are reversible while others are not. More practically, the pathway for electron transport remains a mystery—if the metallic nanoparticles are isolated and dispersed within an insulating medium, how are they electronically connected to the current collector?^{11,12}

A number of metal fluorides, such as FeF₂, FeF₃, and CuF₂, are promising cathode materials (when paired with a prelithiated anode) due to their high energy density and low cost compared to conventional intercalation materials.⁶ Previous investigations of CuF₂ have shown that the lithiation process is irreversible, which is attributed to the direct oxidation of Cu into a soluble phase during the reconversion.² On the other hand, FeF₂ and FeF₃ are highly reversible. Recent studies have shown that the electrochemical lithiation of FeF₃ includes an insertion step and multiple phase transitions, followed by a conversion process.^{6,13,14} In principle, the reaction in FeF₂ is simpler, involving only the conversion step, although the possibility of a small amount of lithium insertion at the early stages of lithiation has not been ruled out.¹⁴ Most of the previous efforts have focused on the thermodynamic aspects of the conversion process;^{2,6,13,14} however, little is known about the microscopic mechanisms involved in the reaction, such as the nucleation and evolution of the LiF and metal phases and their phase distribution on the nanoscale. High-resolution transmission electron microscopy (TEM), which was often used to characterize the structure of the converted phases, provides sufficient contrast only for a fraction of the metallic particles; little contrast is observed for the lithium oxides or fluorides due to the weak scattering of the light constituent elements.^{1,11} Without knowing the spatial correlation among the phases within the converted material and their relationship to the parent phase, the mechanisms for charge and mass transport during the conversion reaction remain elusive.

In this study, we investigated the structure and phase evolution in the binary metal fluorides MF₂ (FeF₂ and CuF₂) on the nanoscale during the first lithiation to better understand the mechanisms underlying the conversion process and the electrochemical behavior. Electron energy-loss spectroscopy (EELS) is extremely sensitive to light elements and was used to generate high-resolution (1 nm scale) compositional images of the primary phases present in the initial and converted electrodes. The local microstructure of the converted metal nanoparticles was examined by atomic z-contrast imaging. In addition, bulk magnetization measurements and X-ray pair-distribution-function (PDF) analysis, both sensitive to short-range order, were used to track the structure

and phase evolution of the electrodes during the conversion process.

MATERIALS AND METHODS

Electrochemical Measurements and Sample Preparation.

The iron fluoride nanoparticles were prepared by the solution-based fabrication process described elsewhere.¹⁵ The synthesized nanoparticles exhibited an ellipsoid shape, approximately 10 nm in diameter and 30 nm in length (representative annular dark field (ADF) and bright field (BF) images of the as-received samples are shown in Figure S1). The FeF₂–C nanocomposites were fabricated by high-energy mechanomilling, with 15 wt.% activated carbon (ASupra, Norit) for 1 h. A total of 1 g of material was loaded into the hardened steel milling-cells in a helium-filled glovebox. After ball milling with the carbon additive, the FeF₂ nanoparticles were smaller (<10 nm) and less regular, according to the PDF analysis (Figure 2) and the TEM images (Figure 6). During the preparation of the electrodes, the FeF₂–C nanocomposite was mixed in acetone with poly(vinylidene fluoride-co-hexafluoropropylene) (Kynar 2801, Elf Atochem), carbon black (Super P, MMM), and dibutyl phthalate (Aldrich), and cast into a tape rinsed in ether to remove the plasticizer. Electrodes that would ultimately be used as TEM samples did not include the binder and were prepared by simply mixing the nanocomposite with 10 wt.% of carbon additive (Super P, MMM). The CuF₂–C nanocomposite was also fabricated by high energy milling the CuF₂ nanoparticles with 15 wt % carbon (Super P, MMM) for 1 h. In preparing the electrode samples for TEM, an additional 10 wt.% of Super P was mixed with the nanocomposite.

Electrochemical measurements of FeF₂–C composite electrodes were performed in galvanostatic mode at both room temperature and 60 °C under a constant current of 4 and 50 mA/g, respectively. Electrochemical cells were prepared in an Ar-glovebox using lithium metal as the counter electrode (half-cell) and a standard electrolyte of 1:1:1 ethylene carbonate (EC)/dimethyl carbonate (DMC)/LiPF₆. Similar conditions were used for the samples prepared for PDF analysis. FeF₂–C samples for TEM and magnetization analysis were cycled at 60 °C under a constant current of 50 mA/g followed by a constant voltage step. The CuF₂–C electrodes for TEM analysis were discharged at 24 °C under a constant current of 7.5 mA/g down to 2 V followed by a constant voltage step for 10 h.

TEM-EELS Measurements. The cycled cells were disassembled in the Ar glovebox and the electrodes were rinsed in DMC and dried under vacuum. Small pieces of the electrode were loaded onto the TEM lacey-carbon grids and sealed in a vacuum transfer holder, and then transferred into the TEM column without air exposure. EELS spectra, selected area electron diffraction (SAED) patterns, and TEM images (with and without energy filtering) were recorded at 300 kV in a JEM-3000F microscope equipped with a Gatan image filter (GIF) spectrometer. The EELS spectra were recorded in diffraction mode (image-coupled) with an energy resolution of ~1.1 eV as measured by the full width at half magnitude (fwhm) of the zero-loss peak (ZLP).

A number of approaches were undertaken to increase the inelastic mean free path and reduce artifacts in the energy-loss images and spectra associated with plural scattering. First, the TEM was operated at a high accelerating voltage of 300 kV, which gives the electrons a long mean-free-path and has been shown to cause less preferential sputtering damage to the lithium in the electrode materials.¹⁶ Importantly, small collection angles were used both in one-dimensional spectroscopy (semiangle $\beta \sim 0.9$ mrad) and two-dimensional mapping (5.0 mrad) by taking advantage of the small characteristic angle (~ 0.1 mrad for Li–K). The two-window ratio method, effective at reducing diffraction and thickness effects, was used for the energy-loss imaging with a pre-edge (background) window of 49–54 eV and postedge windows of 55–60 and 68–73 eV for the Fe–M and Li–K, respectively. A narrow

energy window, 5 eV, was used to reduce the plural scattering effects, while still satisfying the required field of view. In recording the maps for Fe and C in the FeF_2-C nanocomposite samples, the traditional three-window methods were used with 5 and 20 eV window sizes for the Fe M- and C K-edges, respectively. ADF and BF STEM images were recorded using a JEOL 2100F (S)TEM instrument and a dedicated aberration-corrected STEM (Hitachi HD2700C) operated at 200 kV.

X-ray Pair Distribution Function Analysis. The samples for X-ray PDF analysis were recovered from cycled batteries stopped at various states during the first discharge by disassembling them inside an Ar glovebox and scraping the powders from the current collector. The electrodes were washed with DMC and packed in Kapton capillaries for PDF experiments. *Ex situ* total scattering studies were conducted using synchrotron X-rays at the Argonne National Laboratory Advanced Photon Source (beamline 11-ID-B). X-ray scattering data, in transmission geometry, was collected at an energy of 58.26 keV ($\lambda = 0.2127 \text{ \AA}$) on powder samples, using an image plate (Perkin-Elmer amorphous silicon detector). A CeO_2 standard was employed to calibrate the sample-to-detector distance, the detector tilt, angle of rotation, and the zero position.

Magnetization Measurements. The magnetic studies were performed *ex situ* using electrode materials obtained from the electrochemical cells at various stages of the first discharge. The cells were disassembled in a helium glovebox, the cathodes were washed in DMC and dried under vacuum, and the active materials were scraped in a plastic capsule sealed with vacuum grease to prevent air exposure. A SQUID magnetometer (Quantum Design MPMS XL-5) was used to investigate the magnetic properties using the following protocol: first, the remnant magnetic field was quenched to less than 3 mOe using the ultralow field option; then, the sample was cooled to 2 K, whereupon a magnetic field of 10 Oe was applied. Zero-field-cooled magnetization was measured while heating the sample from 2 to 400 K, followed by field-cooled (FC) magnetization measurement of the sample from 400 to 2 K. Magnetization curves were measured at 2 and 298 K in magnetic fields up to 5 T. The sample was zero-field-cooled before the magnetization data was taken at 2 K. Two additional tests were performed on the fully lithiated sample: *ac* magnetic susceptibility was measured from 2 to 300 K after zero-field cooling, *ac* fields of 4 Oe with frequencies from 10 to 10 000 Oe were used; also, the magnetization was measured at 2, 50, 100, 150, 200, 250, and 300 K in magnetic fields up to 9 T using Quantum Design PPMS.

RESULTS

Iron fluoride (FeF_2). Figure 1a shows the voltage profile from the FeF_2-C nanocomposite electrode cycled in galvanostatic mode at room temperature, demonstrating high reversibility after the first discharge. The redox plateau in the first discharge occurs at ~ 1.7 V, much lower than the equilibrium value (~ 2.7 V), while the plateaus in the subsequent discharges increase to 2.3 V. The rise of the FeF_2 redox potential after the first lithiation is attributed to an increase in kinetics, which is due to the reduction in particle size of the reconverted FeF_2 ; similar phenomena were also reported for other conversion compounds.¹ The large hysteresis between the discharge and charge potentials (>0.7 V) is clearly evident. A moderate improvement in the kinetics was achieved by raising the temperature to 60 °C, as shown by the rise of the redox potential to ~ 2 V (closer to equilibrium) in the first discharge (Figure 1b). It is interesting to note that the hysteresis in the subsequent cycles at 60 °C is similar to that at room temperature. However, the undesirable side reactions seem to be more prevalent at 60 °C, as indicated by the multiple plateaus above 2.8 V during charge. These reactions may be associated with the oxidation of iron to a higher valence state, such as Fe^{3+} ,

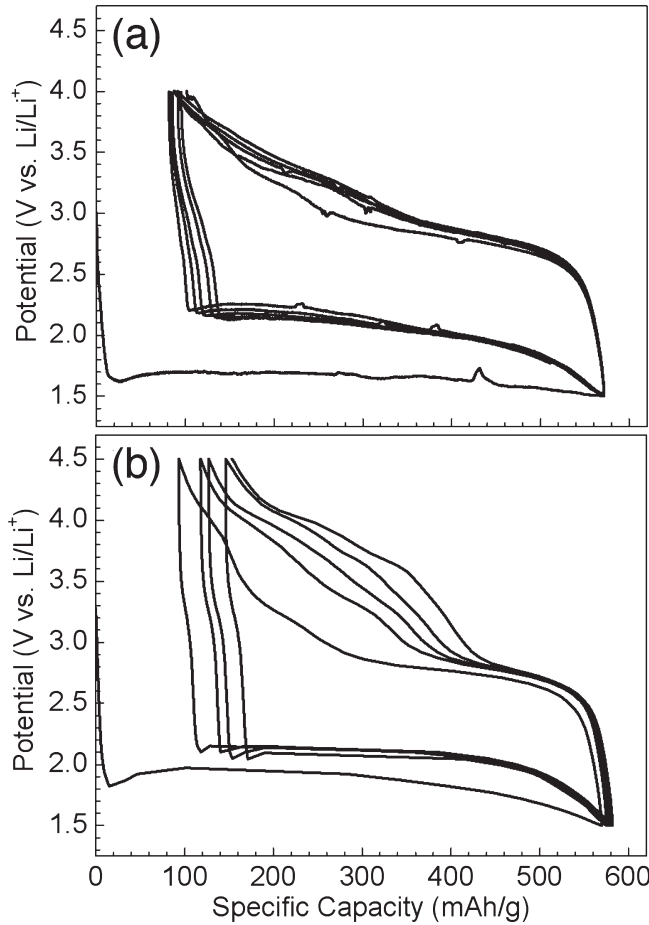


Figure 1. Voltage profiles of the FeF_2-C nanocomposite electrode for the first 5 cycles showing a high reversibility after the 1st discharge at (a) room temperature and (b) 60 °C.

and are likely responsible for the reduction of cycle life observed at elevated temperature.

Synchrotron X-ray diffraction patterns were recorded from the FeF_2-C electrodes at different states of lithiation, as shown by the labels (A–F) in the voltage profile (first discharge) of Figure 2a. The corresponding PDF patterns are given in Figure 2b. At the early stage of lithiation, 0–0.29 mol Li (A–C), the PDF patterns remain unchanged, suggesting that no significant structural modifications have occurred. The nucleation of the converted products should commence at the point of the overpotential (lowest potential between B and C). Before this, the higher voltage region may be due to a host of surface related reactions involving the reduction of iron ($\text{Fe}^{3+} \rightarrow \text{Fe}^{2+}$); these may include anion-deficient regions or surface contamination, although no second phase was detected by XRD. PDF analysis of these samples reveals no significant changes in the refined lattice parameters (Table SI, Supporting Information), confirming that no significant Li intercalation occurred. At low Li concentrations (<0.87 mol) the concentration of Fe is below the detection limit; the first clear signs of α -Fe (Fe–Fe peaks) are observed in sample (D) at 0.87 mol Li. As the discharge reaction proceeds, the α -Fe phase grows at the expense of the FeF_2 .

As the discharge reaction proceeds, the oscillations fall off at progressively lower r -values (seen more clearly in the pattern plotted to 80 Å (Figure S2)). Since the PDF peak intensity

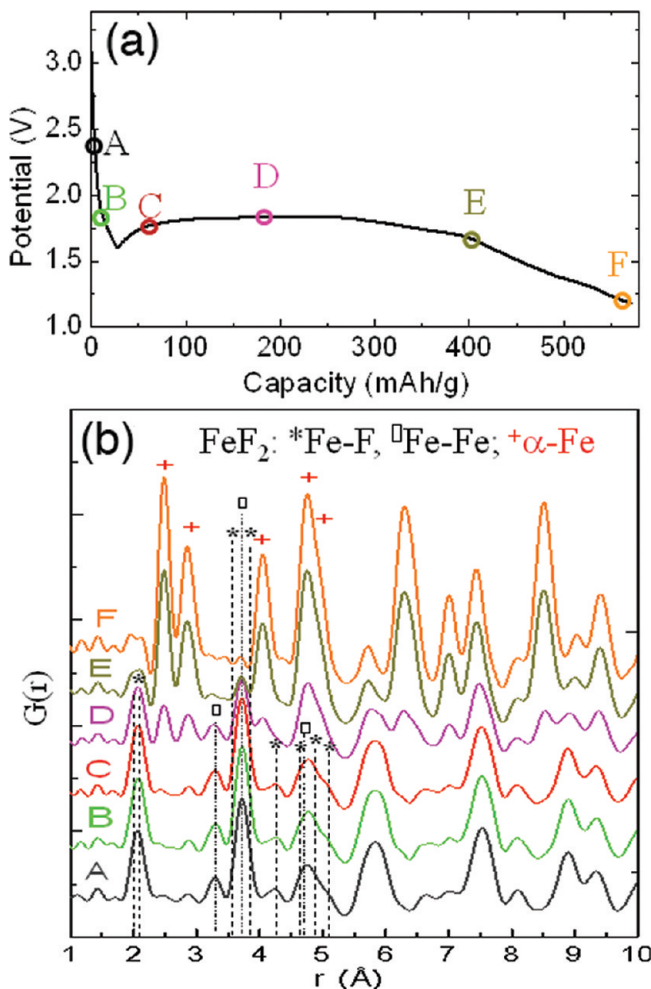


Figure 2. *Ex situ* X-ray PDF analysis of the FeF_2 -C electrode during conversion showing (a) voltage profile for the first discharge (C/100) at various states of lithiation (labeled as A–F) and (b) the corresponding PDF profiles ($G(r)$). The markers in (b) indicate the expected peak positions in FeF_2 (tetragonal $P4_2/mnm$) showing $\text{Fe}-\text{F}$ (*) and $\text{Fe}-\text{Fe}$ (□) bond distances, and in $\alpha\text{-Fe}$ (cubic $I\bar{m}3m$) showing $\text{Fe}-\text{Fe}$ (+) bond distances.

reflects the level of ordering (coherence), the point at which the oscillation magnitude falls to zero is an indication of the extent of long-range order or, in this case, the particle dimensions. Thus, these results suggest a gradual decrease of particle size with lithiation. The PDF fit ($\alpha\text{-Fe}$, $I\bar{m}3m$) of the fully discharged sample (F) with 2 mol of Li (shown in Figure 3) reveals a particle size approaching 2.6 (0.1) nm. However, it is interesting to note that the PDF correlations are not completely damped out at higher r -values. The best fit included a second $\alpha\text{-Fe}$ phase, coherent out to 7.4 (0.2) nm, which indicates a distribution of particle sizes or nonspherical particle shapes.

The conversion reaction was further investigated by magnetization measurements and exploiting the different magnetic properties between Fe and FeF_2 .^{17,18} When paramagnetic FeF_2 converts into superparamagnetic Fe, the linear magnetization curve becomes S-shaped, and the magnetization rapidly increases (Figure 4a). Above 10% lithiation (near point C in Figure 2a), the saturation magnetization increases linearly, consistent with the gradual growth of metallic Fe during the conversion reaction

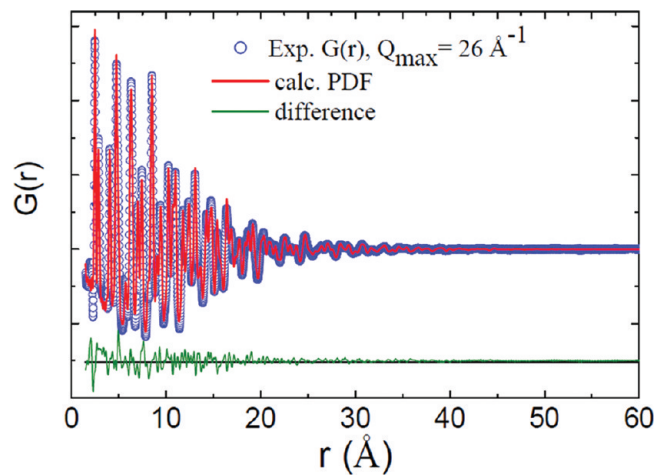


Figure 3. Experimental PDF profile $G(r)$ from the converted Fe nanoparticles along with the calculated PDF determined using two iron phases coherent to 2.6 and 7.4 nm.

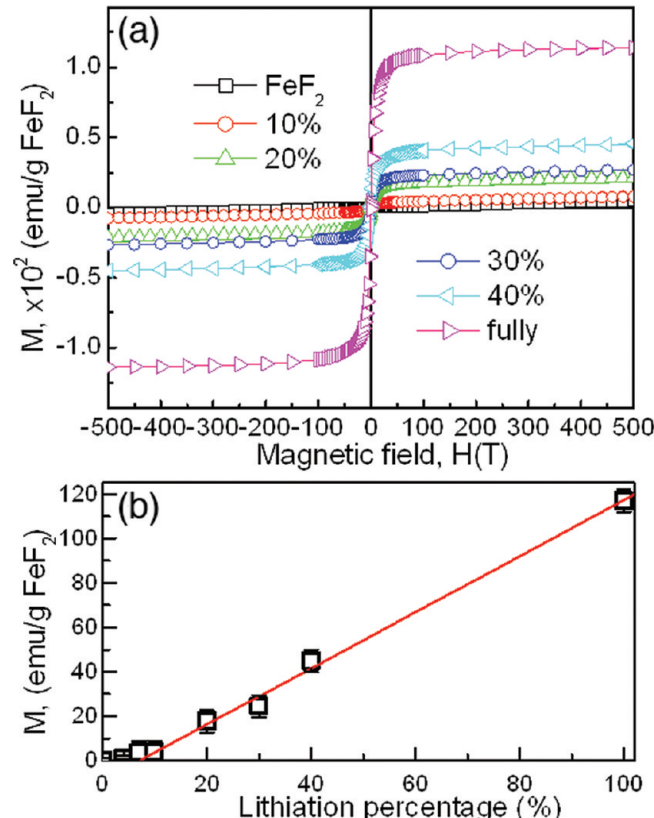


Figure 4. Bulk magnetization measurements of the converted Fe nanoparticles from FeF_2 -C electrodes at different lithiation states, showing (a) dc magnetization (M - H) curve and (b) saturation magnetization values at 298 K.

(Figure 4b). The saturation magnetization corresponds to a magnetic moment of about $1.5 \mu_B$ per Fe atom (typically $2.2 \mu_B$ for bulk Fe) which is typical for superparamagnetic Fe particles.¹⁹ The room-temperature magnetization curves are consistent with the superparamagnetic behavior of $\alpha\text{-Fe}$ since they do not show

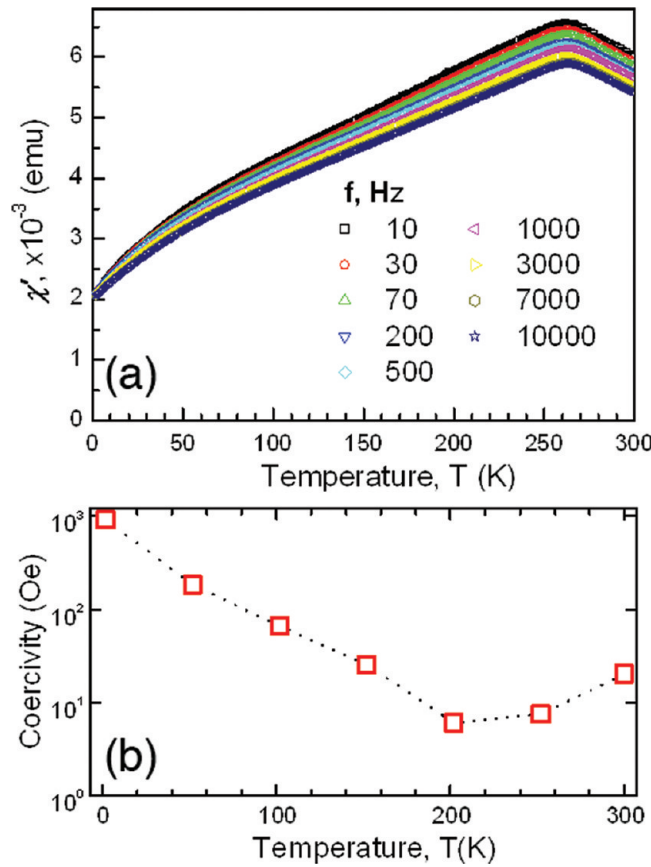


Figure 5. Determination of the magnetic domain size of the converted iron nanoparticles in the fully lithiated electrodes by (a) the temperature dependence of the real component (χ') of the ac susceptibility measured at various frequencies and (b) the temperature dependence of the coercivity.

any significant hysteresis (<10 Oe of coercivity over the entire lithiation process).

Fe nanoparticles clearly exhibit signs of superparamagnetism; however, the behavior is different from that typically observed in superparamagnets composed of noninteracting small particles. For example, the *ac* susceptibility of the fully lithiated sample (Figure 5a) reveals broad maxima centered at 260 K for both real and imaginary components. There is no pronounced shift toward lower temperatures with decreasing *ac* frequency as expected for superparamagnets. In addition, the coercivity (Figure 5b), drops nearly exponentially from about 1000 Oe at 2 K to 10 Oe at 200 K, and then increases slightly. In conventional superparamagnetic particles, coercivity is proportional to the square root of the temperature.¹⁹ An investigation of the susceptibility of the electrode to field cooling (FC) and zero-field cooling (ZFC) at various states of lithiation (Figure S3) revealed broad maxima for FC; while the maxima for the ZFC data appear at ~ 300 K up to 20% lithiation and shift toward higher temperatures with increasing lithium concentration. The ZFC and FC results diverge above 400 K for all samples investigated. From these results, we conclude that the blocking temperature (T_b) in this system is fairly high, ranging from 200 to 400 K, and does not show a clear dependence upon the degree of lithiation. Using the relationship between the T_b and the particle volume (V): $T_b = KV/25k_B$, where $K = 4.8 \times 10^5$ erg/cm³ is the magnetocrystalline energy and $k_B = 1.38 \times 10^{-16}$ erg/K is the Boltzmann constant, we

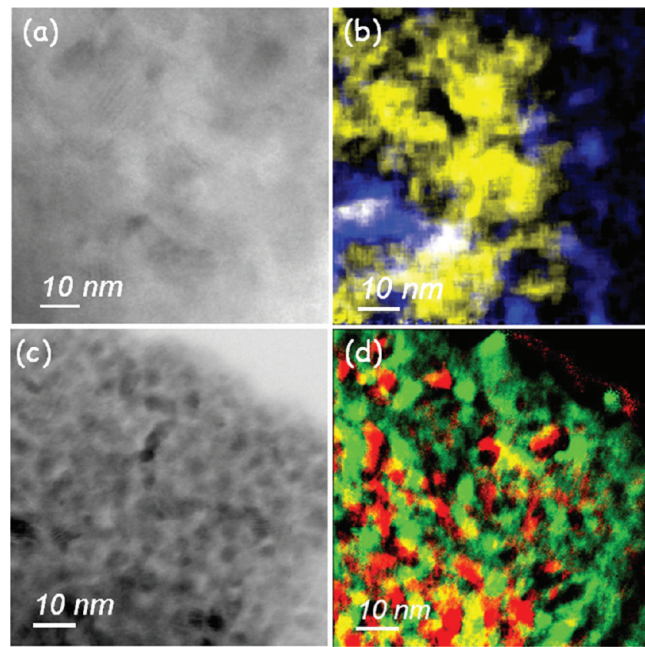


Figure 6. Morphology and spatial distribution of the phases in the initial FeF₂-C nanocomposite electrode: (a) BF TEM and (b) false-color elemental map showing C (blue) and FeF₂ (yellow), along with images from the fully lithiated electrode; (c) BF TEM and (d) false-color elemental map showing Fe (green) and LiF (red).

estimate the magnetic domain size of the Fe particles to be 7–9 nm. This is significantly larger than the 3.2 nm of the Fe particles that is determined from PDF analysis, pointing to the magnetic exchange between individual particles. The characteristic length of the magnetic interactions remains unchanged as lithiation progresses and roughly corresponds to the particle size of the FeF₂ in the initial nanocomposites.

X-ray PDF and magnetization measurements provided detailed information on the structural evolution that occurs during the conversion from FeF₂ to metallic Fe; both suggest that the conversion process dominates the redox reaction and no significant intercalation occurs in the early stages of lithiation. However, neither technique is sensitive to the converted LiF phase. In an attempt to better understand the correlation between the initial FeF₂ phase and the converted phases (i.e., Fe and LiF), TEM imaging, electron diffraction, and EELS were used to investigate the local structure and phase distribution of the nanocomposite electrode before and after lithiation. Figure 6a shows the typical BF image for the initial FeF₂-C nanocomposite electrode, consisting of ~ 10 nm FeF₂ particles (dark contrast) embedded in a carbon matrix (light contrast). To better distinguish FeF₂ from the background of carbon, an elemental map was generated from the same region using the inelastic signal from the Fe M₂₃- and C K-edges. Agglomerates of FeF₂ particles (yellow), wrapped in a carbon matrix (blue), are well resolved (Figure 6b). Figures showing the chemical distribution over a large area and additional details on the procedures used to reconstruct the elemental maps are given in the Supporting Information (Figure S4).

Figure 6c shows a BF TEM image taken from a thin area of a fully lithiated sample, showing the 3–5 nm Fe nanoparticles (dark contrast) on a bright background. The converted LiF particles are barely visible in the BF image, but easily detected by

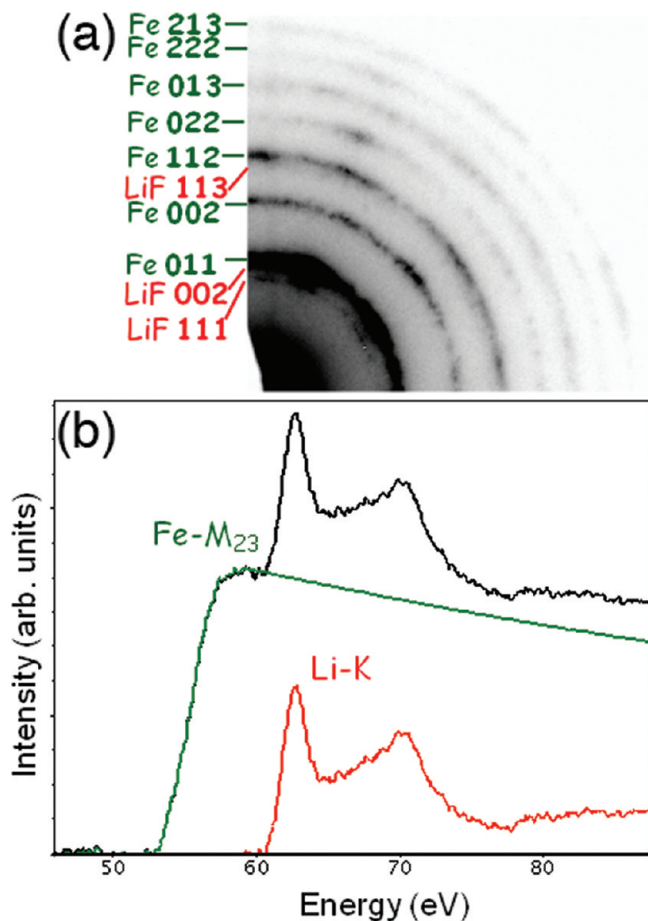


Figure 7. Identification of the Fe and LiF phases in the fully lithiated sample by (a) SAED pattern, along with (b) the energy-loss spectra for Li K- and the Fe M₂₃-edges acquired from the same area as in Figure 6c,d.

the electron diffraction and EELS measurements. In the SAED pattern (Figure 7a) acquired from the same area, intense rings associated with the α -Fe phase were observed, along with two weak rings associated with LiF (111) and (113) reflections (the (002) reflection is overlapped with Fe (011)). The presence of metallic Fe and Li in the form of LiF, was further confirmed by the characteristic near-edge fine structure in the Fe M₂₃- and Li K-edge spectra (Figure 7b). The combination of the bulk X-ray diffraction and magnetization measurements along with the local TEM-EELS measurements provides compelling evidence of a three-phase conversion reaction over the first discharge, namely: $\text{FeF}_2 + 2\text{e}^- + 2\text{Li}^+ \rightarrow \text{Fe} + 2\text{LiF}$. In this complex redox reaction, three nanoscale phases (FeF₂, Fe, and LiF) coexist, in contrast to the two-phases in a traditional intercalation process.

If judged simply from the BF TEM image (Figure 6c), the iron nanoparticles appear to be spherical and isolated from each other. However, the contrast in the BF images can be misleading due to its dependence on grain orientation and crystallinity, along with the weak contrast from the LiF phase. Therefore, the inelastic scattering arising from the Fe-M₂₃ and Li-K excitations was used to map the spatial distribution of Fe and LiF. To limit the undesirable effects from plural plasmon scattering, a region with a low concentration of carbon black was chosen for these measurements. The energy-filtered images shown in Figure 6d were constructed using the two-window ratio method (additional details

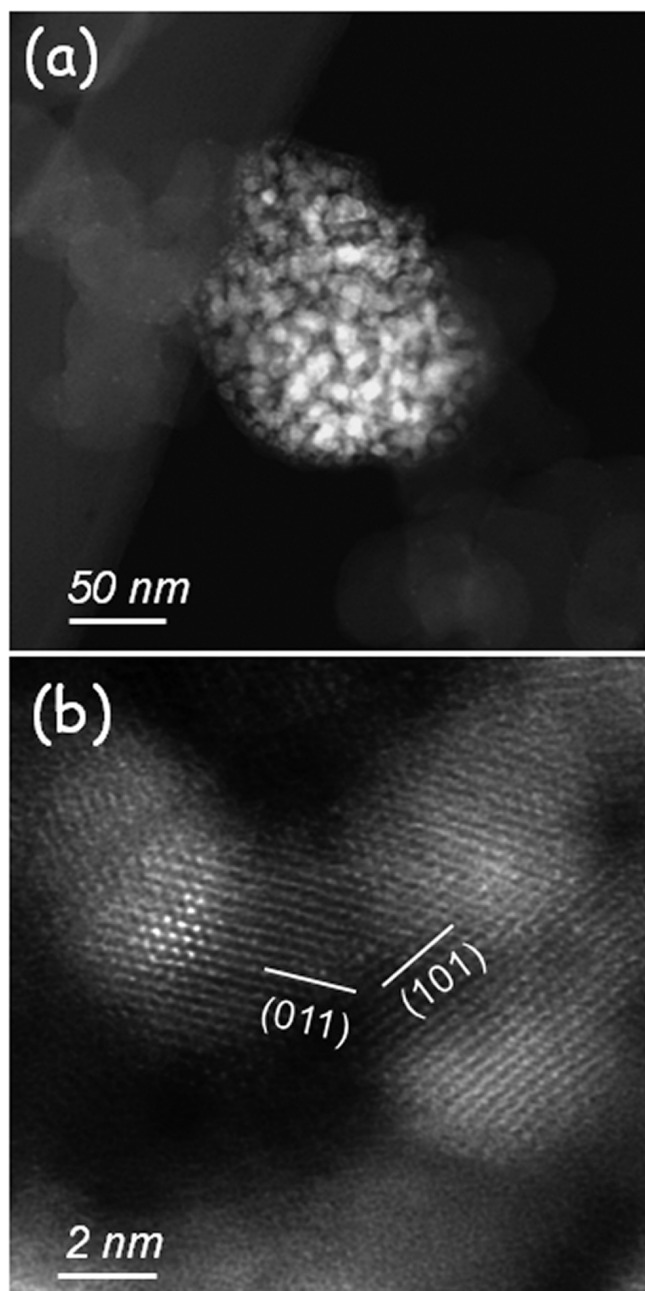


Figure 8. Local structural analysis of the converted Fe particles in the fully lithiated electrode by high-angle annular dark-field (HAADF) images showing (a) a single agglomerated secondary particle at a low magnification, and (b) the structural coherence between neighboring particles at a high magnification, viewed along the [111] direction.

on the procedures are given in the Supporting Information, Figure S5). The false-colored composite image, with Fe in green color and LiF in red, reveals a high spatial correlation between the two phases, which are closely interwoven with each other across the full field of view. Closer inspection reveals that the irregular-shaped iron nanoparticles are interconnected, forming a bicontinuous network, and are not isolated as they appear to be in the BF image (Figure 6c).

The phase distribution shown in Figure 6d reveals roughly similar amounts of Fe and LiF; however, based on a stoichiometric reaction, the amount of LiF in the converted electrode

should be twice that of Fe. The observed deficiency in the LiF phase is attributed to radiation damage (via fast radiolysis), which is a frequent challenge when investigating lithium-containing materials by TEM-EELS. However, beam damage to the Fe nanoparticles, via sputtering, is expected to be negligible due to the small displacement cross section (calculated using the Mott model, shown in Figure S6).¹⁶

The local structure of iron nanoparticles in the converted electrode was further examined by high-angle annular dark-field (HAADF) images (Figure 8). The small iron nanoparticles are distinguishable from the carbon black and other components of the electrode as a result of the strong dependence of the contrast on atomic number, z (intensity scales as $\sim z^{1.6}$ with a collection angle of 3 times the convergent angle). The HAADF image in Figure 8a reveals a bright secondary particle (~ 150 nm in diameter) composed of many small iron nanoparticles, with sizes varying from subnanometer to a few nanometers. Interestingly, the small Fe particles (≤ 1 nm) are mostly distributed in the near-surface region of the secondary particle. It is likely that these particles form at the early stages of lithiation and remain small due to the limited iron available for growth at this stage of the reaction. The darker particles in the image are carbon black. Clearly, the Fe nanoparticles were not converted from a single particle but rather an agglomerated secondary particle of FeF_2 , as shown in Figure 6b.

An atomic-scale image of a few individual iron particles (Figure 8b), obtained using a dedicated aberration-corrected STEM, clearly reveals that some of the iron nanoparticles (3–5 nm in diameter) are interconnected through their common {110} planes. The coherent particles sharing a common crystallographic orientation may be converted from a single FeF_2 particle. It is likely that the rapid migration of fluorine out of the FeF_2 lattice allows the iron particles to nucleate and grow with some preferred alignment with the parent crystal in order to reduce the interfacial energy. Although further theoretical and experimental verification is needed, this local observation is consistent with the findings from X-ray PDF, magnetization, and the EELS chemical mapping, providing strong evidence for the formation of a bicontinuous Fe network during conversion.

Copper Fluoride (CuF_2). The CuF_2 –C nanocomposite is similar to the FeF_2 –C electrode (Figure 6a,b), forming agglomerates of CuF_2 nanoparticles (bright) surrounded by carbon black (dark). Figure 9a shows typical HAADF STEM images of the ball-milled CuF_2 –C nanocomposite. Although a high electrochemical capacity was measured with this sample (Supporting Information, Figure S7), the lithiation reaction was irreversible.^{2,7} Characterization of the converted phases by electron diffraction and EELS confirmed the direct conversion of CuF_2 into Cu and LiF with no intercalation step (not shown here), which is consistent with previous reports.^{2,7,20} Figure 9b depicts a typical BF TEM image from the fully lithiated electrode, showing plate-like and spherical Cu nanoparticles with sizes ranging from 5 to 12 nm. The STEM-EELS map (Figure 9c) reveals the clear separation of the converted Cu particles (green) from the LiF phase (red), which seems to segregate to the surface. Although the converted Cu nanoparticles are highly crystalline, local defects, such as stacking faults, are common, as illustrated by the blue and red lines in the high resolution HAADF STEM image of Figure 9d. These observations suggest a slightly different conversion process for CuF_2 than for FeF_2 , which will be discussed below.

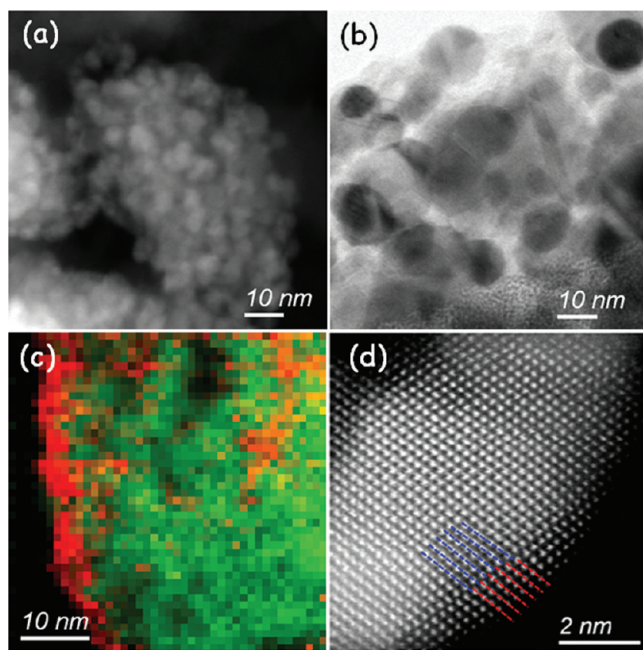


Figure 9. Local structure and phase distribution of CuF_2 –C electrodes at the initial and fully lithiated states showing (a) ADF-STEM image of initial electrode; (b) BF-TEM image after lithiation; (c) false-color composite image of the converted electrode showing LiF (red) and Cu (green) phases; (d) HAADF atomic image of a single converted Cu particle, with red and blue lines highlighting a stacking fault.

DISCUSSION

A schematic illustration of the nano FeF_2 agglomerates (yellow) in the initial state is shown in Figure 10 (left). The large surface area and energy of the constituent nanoparticles (i.e., FeF_2 and C) make it difficult to uniformly disperse one phase into another; the heterogeneous nature of the electrode is seen in Figure 6b. Before lithiation, the FeF_2 nanoparticles tend to form agglomerates, making the pathway for electron transport much longer than the size of the primary particles. Furthermore, a large interfacial resistance may create a barrier for electron transport, which could also help explain the poor kinetics in the initial lithiation. Agglomeration is a common issue with nanocomposite electrodes and may be alleviated somewhat by designing nanostructured electrodes in which individual active nanoparticles are directly connected to the current collector. Tarascon et al. recently used this approach to achieve a high rate capability with nanostructured Fe_3O_4 .²¹

The nucleation and growth of the Fe and LiF from the FeF_2 precursor, via a complex solid-state reaction, involves both charge and mass transport. Diffusion of the cations (i.e., Li^+ and Fe^{2+}) and anions (F^-), and the electronic and ionic conductivity of all the phases must be taken into account in explaining the morphology and spatial correlation of the new phases. First, the Fe^{2+} ion is much less mobile than Li^+ and F^- , and may be reduced to Fe^0 at, or close to, its initial atomic sites in the parent FeF_2 upon reacting with Li^+ . Therefore, the converted Fe particles may take the form of the skeleton structure occupying almost the same space as the FeF_2 precursor. The remaining voids within the skeletal Fe are filled with the crystallized LiF. In contrast, the F^- ion, with its higher diffusivity, should more readily migrate out from a minimal depth within the FeF_2 lattice toward the surface, where it forms LiF upon reacting with Li^+ from the electrolyte. This scenario is

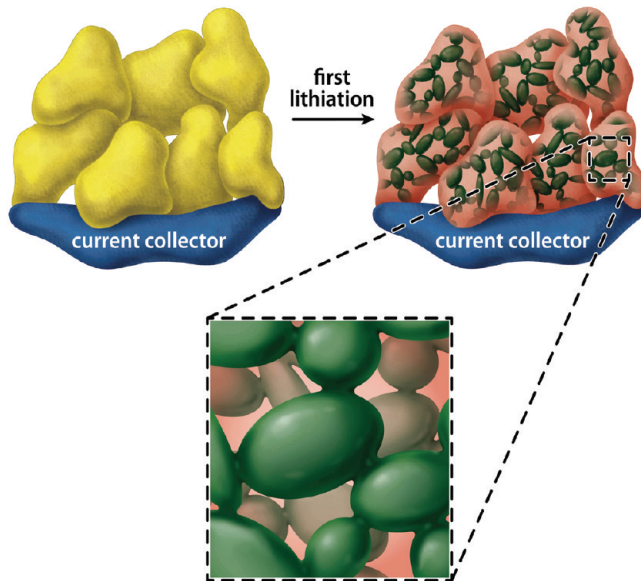


Figure 10. Schematic illustration for the conversion of the FeF₂ agglomerates (yellow; left) into a bicontinuous network of Fe nanoparticles (green) and LiF (red) that forms within the same domain of parent FeF₂ during the 1st lithiation (right). The 3D character of the iron network is depicted in the expanded region (bottom). In this illustration, the carbon is assumed to be part of the current collector.

consistent with the detection of the large LiF crystals by XRD in the early stage of the discharge.¹¹ Nevertheless, the F⁻ ions do not move too far from their original location within the agglomerate, as depicted in Figure 6d; this is likely due to the relatively fast diffusion of the Li⁺ along the boundaries between the Fe and the newly formed LiF phase. Magnetization measurements (Figure 5) clearly show that the magnetically coupled Fe particles do not change with lithiation, denoting that the length scale of the magnetic interactions stays almost the same over the whole conversion process. These results are consistent with bulk X-ray PDF measurements (Figure 3), local EELS mapping (Figure 6), and z-contast imaging (Figure 8), and indicate the formation of a bicontinuous Fe network surrounded by LiF, that grows within the domains of the parent FeF₂ particles during the first lithiation. Figure 10 illustrates this process.

The bicontinuous Fe network clearly acts as a pathway for electron transport; however, the mechanism for ion transport is less obvious since the surrounding LiF is an ionic insulator. Rapid F⁻ transport would likely result in a porous electrode morphology with an inhomogeneous distribution of LiF on the surface and in the bulk. However, the EELS maps clearly show the LiF grows deep within the nanostructure, and is not formed on the surface, which seems to indicate that Li⁺, rather than F⁻, is responsible for the primary ion transport. The diffusion of the Li⁺ likely occurs through the massive interface formed between the nanoparticulate phases (i.e., LiF and Fe), similar to that proposed for bismuth fluoride (BiF₃).¹² However, the mechanism for electron transport in BiF₃ appears to differ from what is presented here for FeF₂, as suggested by the presence of pseudo plateaus in the voltage profiles.¹²

The formation of the bicontinuous Fe network during the first lithiation occurs via a nonequilibrium process, during which a large overpotential (~ 0.8 V) is necessary to overcome barriers of charge and mass transport in the FeF₂ agglomerates (as shown in

Figure 1), even at a low cycling rate (equivalent to C/150). A substantially smaller overpotential (~ 0.3 V) is required in the subsequent lithiation, due to the reduction in size of the reconverted FeF₂ particles to less than 5 nm as determined from TEM (Figures S8a,b). A slightly smaller size, ~ 2.4 (0.2) nm on average, was obtained from X-ray PDF analysis (Figure S8c); but this may be an underestimate due to structural disorder. The network of interconnected Fe nanoparticles (for electron transport) along with the massive interface between the Fe and LiF (for ion transport) facilitates reconversion. The unique nanomorphology of the converted phase may also explain the asymmetry observed between the lithiation and delithiation reactions, the latter being much faster.

The reversibility of the lithium conversion reactions in metal oxides and fluorides was ascribed to the formation of fine metallic nanoparticles embedded in an insulating lithium oxide or fluoride matrix, with a high metal–matrix contact interface.¹ However, this model was based on observations of converted metallic nanoparticles in BF TEM images and the assumption that the individual metallic nanoparticles were wrapped in the invisible lithium oxide or fluoride. This observation does not explain how electron transport occurs through the highly insulating media of the lithium fluoride or oxide. Interestingly, some evidence for electronic percolation was observed in the lithium conversion products (metallic nanoparticles and Li₂O) obtained from metal oxides (e.g., NiO) in which there was a high content of the metal.²² The EELS map in Figure 6d clearly shows the distribution of both phases (LiF and Fe) in the converted (lithiated) electrode, and reveals their close proximity and the bicontinuous network of iron nanoparticles. In accordance with our observations, the conductive carbon additive helps to preserve the electronic integrity of the whole electrode, but may not be critical for the reversibility of the electrode. Instead, the formation of a bicontinuous iron network, which provides a large LiF/Fe interface area and a highly conductive pathway for local electron transport, appears to be the crucial component that facilitates the conversion in subsequent cycles.

In contrast to FeF₂, the converted product from CuF₂ consists of larger Cu nanoparticles, isolated from the LiF phase (Figure 9). This important morphological difference may help explain the lack of reversibility in CuF₂. Although other factors, such as the oxidation of Cu into a soluble phase, likely play an important role, the absence of a pathway for electron transport prevents the facile reconversion of the CuF₂ during delithiation. The morphological difference in the conversion products of FeF₂ and CuF₂ is in part attributed to the difference in the diffusivity of the cations (i.e., Cu²⁺ versus Fe²⁺). The Fe²⁺ ions are slow, leading to the nucleation and growth of Fe into small particles near the parent phase, while the Cu²⁺ ions are faster and tend to move away from the parent phase, resulting in coarsened Cu particles.

CONCLUSION

A comprehensive study of the electrochemical lithiation of metal fluorides MF₂ (M = Fe and Cu) revealed new insights into the structural and morphological changes occurring during conversion, the pathways for electron and ion transport, and the spatial distribution of the converted phases. Lithiation of MF₂ occurs via a three-phase conversion process, $MF_2 + 2Li^+ + 2e^- \rightarrow 2LiF + M$, with no intercalation involved. The reaction in FeF₂ leads to the formation of a bicontinuous Fe network embedded in an insulating LiF matrix, which provides a pathway for local electron transport; while the massive interface between the

nanostructured phases provides a pathway for ion transport during the conversion process. These results offer some experimental evidence explaining the origin of the high lithium reversibility in FeF_2 . A similar investigation performed on CuF_2 revealed a slightly different scenario, namely, the formation of larger Cu particles separated by the LiF phase. The differences in the nanomorphology and phase distribution, possibly due to the higher diffusivity of the Cu^{2+} (compared to Fe^{2+}), may account for the poor reversibility in the CuF_2 system.

■ ASSOCIATED CONTENT

S Supporting Information. Morphology of the synthesized FeF_2 , PDF analysis, magnetization measurements, TEM-EELS elemental maps, sputtering damage, and electrochemistry of the CuF_2-C composite electrode. This material is available free of charge via the Internet at <http://pubs.acs.org>.

■ AUTHOR INFORMATION

Corresponding Author
graetz@bnl.gov

■ ACKNOWLEDGMENT

This work was supported by the Northeastern Center for Chemical Energy Storage, an Energy Frontier Research Center funded by the U.S. DOE, BES under award No. DE-SC0001294. TEM studies carried out at Brookhaven National Laboratory was partially supported by the U.S. Department of Energy, Office of Basic Energy Sciences, Materials Science and Engineering Division, and through the use of Center for Functional Nanomaterials under Contract No. DE-AC02-98CH10886. The Generalitat de Catalunya is gratefully acknowledged for the Postdoctoral research grant awarded to R. Robert (BP-DGR 2008). FW thanks NSERC of Canada for a fellowship. We thank Karena Chapman and Peter Chupas for their help with data collection and analysis at 11-ID-B at the Advanced Photon Source, and Tiffany Bowman for help with the graphic in Figure 10. We thank Anton van der Ven and Gerbrand Ceder for insightful discussions.

■ REFERENCES

- (1) Poizot, P.; Laruelle, S.; Gruegeon, S.; Dupont, L.; Tarascon, J.-M. *Nature* **2000**, *407*, 496.
- (2) Badway, F.; Mansour, A. N.; Pereira, N.; Al-Sharab, J. F.; Cosandey, F.; Plitz, I.; Amatucci, G. G. *Chem. Mater.* **2007**, *19*, 4129.
- (3) Oumella, Y.; Rougier, A.; Nazri, G. A.; Tarascon, J. M.; Aymard, L. *Nat. Mater.* **2008**, *7*, 916.
- (4) (a) Balaya, P.; Li, H.; Kienle, L.; Maier, J. *Adv. Funct. Mater.* **2003**, *13*, 621. (b) Poizot, P.; Laruelle, S.; Gruegeon, S.; Tarascon, J.-M. *J. Electrochem. Soc.* **2002**, *149*, A1212.
- (5) (a) Pereira, N.; Dupont, L.; Tarascon, J.-M.; Klein, L. C.; Amatucci, G. G. *J. Electrochem. Soc.* **2002**, *150*, A1273. (b) Pereira, N.; Klein, L. C.; Amatucci, G. G. *J. Electrochem. Soc.* **2002**, *149*, A262.
- (6) (a) Badway, F.; Cosandey, F.; Pereira, N.; Amatucci, G. G. *J. Electrochem. Soc.* **2003**, *150*, A1209. (b) Badway, F.; Cosandey, F.; Pereira, N.; Amatucci, G. G. *J. Electrochem. Soc.* **2003**, *150*, A1318. (c) Plitz, I.; Badway, F.; Al-Sharab, J.; DuPasquier, A.; Cosandey, F.; Amatucci, G. G. *J. Electrochem. Soc.* **2005**, *152*, A307. (d) Bervas, M.; Badway, F.; Klein, L. C.; Amatucci, G. G. *Electrochem. Solid-State Lett.* **2005**, *8*, A179. (e) Bervas, M.; Klein, L. C.; Amatucci, G. G. *J. Electrochem. Soc.* **2006**, *153*, A159.
- (7) Yamakawa, N.; Jiang, M.; Grey, C. P. *Chem. Mater.* **2009**, *21*, 3162.
- (8) Cabana, J.; Monconduit, L.; Larcher, D.; Palacín, M. R. *Adv. Mater.* **2010**, *22*, E170.
- (9) Tarascon, J.-M. *Philos. Trans. R. Soc., A* **2010**, *368*, 3227.
- (10) Yu, X. Q.; Sun, J. P.; Tang, K.; Huang, X. J.; Dupont, L.; Maier, J. *Phys. Chem. Chem. Phys.* **2009**, *11*, 9497.
- (11) Li, H.; Balaya, P.; Maier, J. *J. Electrochem. Soc.* **2004**, *151*, A1878.
- (12) Bervas, M.; Mansour, A. N.; Yoon, W. S.; Al-Sharab, J. F.; Badway, F.; Cosandey, F.; Klein, L.; Amatucci, G. G. *J. Electrochem. Soc.* **2006**, *153*, A799.
- (13) Doe, R. E.; Persson, K. A.; Meng, Y. S.; Ceder, G. *Chem. Mater.* **2008**, *2*, 5274.
- (14) Yamakawa, N.; Jiang, M.; Key, B.; Grey, C. P. *J. Am. Chem. Soc.* **2009**, *131*, 10525.
- (15) Pereira, N.; Badway, F.; Wartelsky, M.; Gunn, S.; Amatucci, G. G. *J. Electrochem. Soc.* **2009**, *156*, A407.
- (16) Wang, F.; Graetz, J.; Moreno, M.; Ma, C.; Wu, L.; Volkov, V.; Zhu, Y. *ACS Nano* **2011**, *5*, 1190.
- (17) Stout, J. W.; Catalano, E. *J. Chem. Phys.* **1955**, *23*, 1803.
- (18) Kumar, D.; Narayan, J.; Kvit, A. V.; Sharma, A. K.; Sankar, J. *J. Magn. Magn. Mater.* **2001**, *232*, 161.
- (19) Fonseca, F. C.; Goya, G. F.; Jardim, R. F.; Mucillo, R.; Carreno, N. L. V.; Longo, E.; Leite, E. R. *Phys. Rev. B* **2002**, *65*, 104406.
- (20) Mansour, A. N.; Badway, F.; Yoon, W. S.; Chung, K. Y.; Amatucci, G. G. *J. Solid State Chem.* **2010**, *183*, 3029.
- (21) Taberna, P. L.; Mitra, S.; Poizot, P.; Simon, P.; Tarascon, J.-M. *Nat. Mater.* **2006**, *5*, 567.
- (22) Sauvage, F.; Tarascon, J.-M.; Baudrin, E. *J. Phys. Chem. C* **2007**, *111*, 9624.